J. Appl. Comput. Mech., xx(x) (2026) 1-11
DOI: 10.22055/jacm.2026.49339.5910

ISSN: 2383-4536
jacm.scu.ac.ir

Shahid Chamran University of Ahvaz

Journal of Applied and Computational Mechanics

Research Paper

Thermal-Induced Intragranular Residual Stresses in LPBF AlSi10Mg and Their Impact on Mechanical Response

Ekaterina Dymnich, Varvara Romanova, Valeriy Shakhidzhanov, Vasiliy Balokhonov, Anzhelika Borodina, Ruslan Balokhonov

Panin Institute of Strength Physics and Materials Science of Siberian Branch of Russian Academy of Sciences, Tomsk, 634055, Russia
E-mail: dymnich@ispms.ru (E.D.); varvara@ispms.ru (V.R.); shakhidzhanov@ispms.ru (V.Sh.); vbalokhonov@ispms.ru (V.B.); anzhelika.borodina.00@bk.ru (A.B.); rusy@ispms.ru (R.B.)

Received May 09 2026; Revised June 23 2026; Accepted for publication June 24 2026.
✉ Corresponding author: E. Dymnich (dymnich@ispms.ru)

Abstract. This numerical study investigates the effect of thermal cycling inherent to laser powder bed fusion on the type III residual stresses and the deformation behavior of an AlSi10Mg alloy at the microscale. Microstructure-based finite element models representing sub-grain cellular-dendritic structures with continuous and discontinuous Si-rich networks are developed from experimental data. The eutectic network morphology strongly governs stress redistribution, strain localization, and the formation of type III residual stresses. A continuous Si-rich network promotes higher residual stresses, generating stress levels approximately 40% greater than those in a discontinuous network, and more distributed plastic strain. A discontinuous network leads to pronounced plastic strain localization between silicon particles. Subsequent tensile simulations demonstrate that plastic strain pre-accumulated during thermal cycling increases flow stress and reduces ductility. The results provide a mechanistic explanation of anisotropic mechanical behavior of an LPBF AlSi10Mg alloy and highlight the critical role of sub-grain microstructural morphology in material performance.

Keywords: Laser powder bed fusion, Si-rich eutectic, Type III residual stresses, Thermal cycling, Micromechanics.

1. Introduction

Laser powder bed fusion (LPBF) is an additive manufacturing technology used for producing geometrically complex components for engineering applications [1–4]. The mechanical properties of as-built LPBF parts exhibit pronounced heterogeneity due to the non-equilibrium nature of the process, which involves heating and cooling at rates exceeding 10^6 K/s, high thermal gradients, and thermal cycling during layer-by-layer fabrication [5–7]. These conditions result in a hierarchical microstructure that differs from that of conventionally processed alloys [5, 8].

LPBF materials exhibit structural hierarchy across multiple length scales [9, 10]. At the macroscale, overlapping laser tracks form characteristic melt pool patterns referred to as a fish-scale pattern. At the mesoscale, epitaxial solidification under high thermal gradients produces columnar grains with a pronounced crystallographic texture. At the micro- or sub-grain scales, rapid solidification leads to the formation of a cellular-dendritic structure [11]. In additively produced Al-Si alloys, primary α-Al cells with characteristic sizes of 200–500 nm are surrounded by a eutectic Si-rich network that restricts dislocation motion and thus contributes to the high strength of the alloy [12–15].

Generally, the cellular-dendritic structure is spatially heterogeneous [5, 8, 9]. Variations in local thermal history within a single melt pool result in three characteristic microstructural regions: a central region with fine columnar cells, a peripheral region with coarser and more equiaxed cells, and a narrow heat-affected zone (HAZ) where the eutectic network is partially broken [8, 12, 16]. These microstructural characteristics lead to a specific local mechanical response [17, 18]. As a result, as-built LPBF AlSi10Mg exhibits high tensile (350–450 MPa) and yield (200–350 MPa) strengths, while its ductility is limited and scattered (1–8%) [16, 19–24].

Another distinct feature of the LPBF process is residual stresses developing across multiple length scales. Of particular interest are type III residual stresses generated from incompatible thermal contraction and plastic deformation between the α-Al matrix and Si-rich network during thermal cycling [25–28]. However, the role of type III residual stress is under discussion due to contradictory reports. While some studies suggested they contributed to strengthening [26], others indicated they may promote crack initiation under loading [29, 30]. In contrast, compressive type III residual stresses have been reported to retard crack propagation [31].

Despite the acknowledged significance, the relationship between cellular-dendritic morphology and the evolution of type III residual stress during LPBF thermal cycling remains insufficiently quantified. Experimental characterization of type III residual stresses is limited by spatial resolution, as the X-ray diffraction measurement inherently averages the stress over a gauge volume much larger than the characteristic cell size [25–28]. Consequently, microstructure-based numerical modeling provides an effective

Published online: August 28 2026

approach for studying these phenomena. Finite-element models that explicitly represent cellular-dendritic structures and their spatial variations allow simulation of thermo-mechanical loading at the microscale and enable direct evaluation of stress and strain partitioning, plastic strain accumulation, and the resulting residual stress state [4, 20, 32–36].

The deformation behavior of additively manufactured AlSi10Mg is strongly affected by both the cellular-dendritic morphology and the type III residual stresses generated during thermal cycling. Because these features are highly heterogeneous at the microscale, homogenized approaches cannot adequately capture the underlying deformation mechanisms. Thus, micromechanical numerical modeling with an explicit representation of sub-grain microstructural features provides an effective framework for linking local thermal history, microstructure, and mechanical response.

In the present work, representative microstructural models corresponding to different melt pool regions are subjected to LPBF-relevant thermal cycling, followed by simulated uniaxial tensile loading. The study aims to quantify the evolution and final distribution of type III residual stress and to clarify their role in the subsequent deformation behavior as a function of local microstructural morphology. The grain structure is intentionally disregarded to study the individual influence of the intragranular morphology on the stress-strain state and to isolate it from any potential grain-scale effects.

This paper is organized as follows. Section 2 describes the LPBF process, methods of microstructural characterization and discusses the experimental results on the intragranular structure of additively produced AlSi10Mg. Section 3 details the development of finite-element models and constitutive equations. Section 4 covers thermo-mechanical analysis of the stress-strain evolution at the microscale. Section 4.1 focuses on the stress-strain state evolution under thermal cycling exploring the Si-rich eutectic effects. Section 4.2 addresses the effect of predefined type III residual stresses on the stress-state state at the microscale. The main findings are summarized in the Conclusion.

2. Microstructure Characterization

A comprehensive description of the LPBF processing and a detailed multiscale structure characterization have been reported in our previous work [37]. In the present study, the discussion of experimental results is limited to aspects directly relevant to the development of the microstructure-based model. The study focuses on the cellular-dendritic microstructure formed in LPBF-manufactured AlSi10Mg components. Figure 1 schematically illustrates the relationship between the LPBF-fabricated part and the resulting cellular microstructure.

Specimens were fabricated from gas-atomized AlSi10Mg powder (average size ~30 μm) using an ONSINT AM150 LPBF system. Key process parameters included a laser power of 200 W, scan speed of 1200 mm/s, hatch spacing of 110 μm, and layer thickness of 30 μm. A bidirectional scanning strategy with a 90° rotation between layers was used, and the platform was preheated to 150 °C to mitigate stresses. The resulting samples exhibited a high relative density of 99.5–99.7%. Microstructural characterization was carried out using transmission electron microscopy (TEM), optical metallography, and energy-dispersive X-ray spectroscopy (EDS).

The cellular-dendritic structure was investigated using optical microscopy and TEM (Figs. 1(c) and 1(d), 2 and 3)). The analyses revealed elongated α-Al cells separated by a continuous Si-rich eutectic walls with undissolved Si particles (Figs. 1(c)-(d) and Fig. 2). EDS mapping showed that more than 80% of the silicon is concentrated within the eutectic phase in the form of particles with characteristic sizes of several tens of nanometers (Fig. 2). Mg is distributed uniformly throughout the α-Al matrix (Fig. 2(d)).

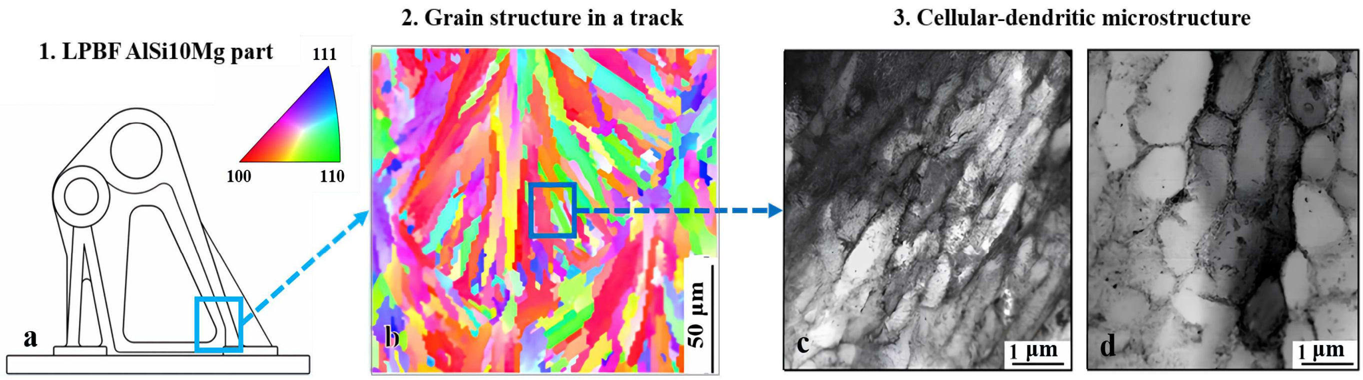

Fig. 1. (a) Multiscale representation of the LPBF AlSi10Mg alloy: schematic example of a complex engineering component, (b) EBSD inverse pole figure map showing the grain structure of the LPBF AlSi10Mg alloy [37], (c) bright-field TEM images of the cellular dendritic structure in LPBF AlSi10Mg alloy in cross-sections which are perpendicular, and (d) parallel to the plane of the build direction.

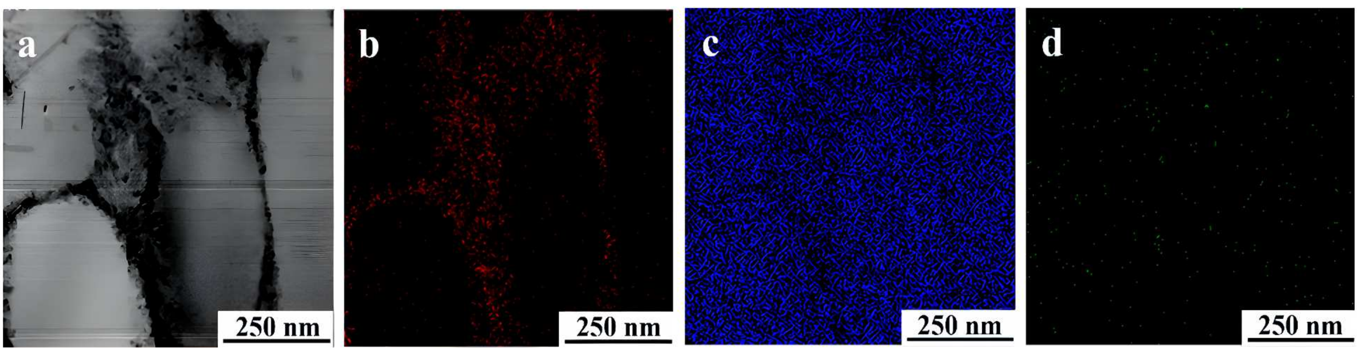

Fig. 2. (a) TEM image of a dendritic cell in the track cross-section, (b) EDS maps of Si, (c) Al, (d) Mg distributions in an additively produced AlSi10Mg alloy [37].

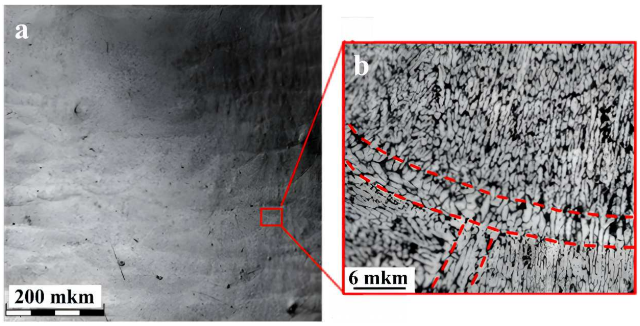

Fig. 3. (a) Optical micrograph of the etched sample side surface with ×20, (b) ×100 magnification (dashed lines indicate the boundaries of the laser tracks).

Pronounced spatial variations in the cell size and morphology are observed within individual melt pools, in agreement with previous studies (Fig. 3). As discussed by Liu et al. [38], this zonal microstructural distribution originated from non-stationary solidification conditions inherent to the LPBF process. A narrow HAZ is present near melt pool boundaries, where the eutectic network is partially dissolved or coarsened. Temperature fields between the liquidus and solidus promote partial remelting and coarsening of the cellular-dendritic structure, whereas sub-solidus reheating of previously solidified layers leads to eutectic breakdown in the HAZ. Further inward, a transition region is characterized by coarser and more equiaxed dendritic cells. The central part of the track is dominated by fine, elongated cells aligned with the local thermal gradient with the lengths along the major and minor axes reaching 1–2 µm and 300–500 nm, respectively (Fig. 3(b)).

3. Model Description

Microstructural models of additively manufactured AlSi10Mg were developed based on TEM data. The initial digital geometry was obtained by binarization of an experimental micrograph of the cellular-dendritic structure. This binarized image served as the baseline model with a discontinuous eutectic network (Fig. 4(b)). A model with a continuous network (Fig. 4(a)) was generated by filling and merging disconnected regions in the baseline model to isolate the effect of eutectic network morphology while excluding geometric variability. This approach preserves the cellular geometry, ensuring that the two models differ only in the continuity of the eutectic network. The Si-rich eutectic wall thickness in the continuous model was then adjusted to maintain a constant volume fraction of Si across both configurations. The resulting geometries correspond to the central melt-pool region (continuous network) and the HAZs (discontinuous network). Both models were discretized using uniform voxel-based finite-element meshes with a resolution of 624 × 532 elements.

Each model was subjected to thermal cycling following the scheme of the temperature profile shown in Fig. 4(c). Owing to the small size of the computational domain, heat conduction was neglected and the temperature was assumed to be spatially uniform. The subsequent uniaxial tensile simulation then served to quantify the impact of the resulting residual thermal stresses.

Thermo-mechanical simulations were performed using a dynamic formulation. The constitutive responses of Al and Si-rich eutectic phases were described using the Duhamel–Neumann relation:

$$\dot{\sigma}_{ij} = -\dot{P}\delta_{ij} + \dot{S}_{ij} = K(\dot{\varepsilon}_{kk} - 3\alpha\dot{T})\delta_{ij} + 2\mu(\dot{\varepsilon}_{ij} - \dot{\varepsilon}_{kk}\delta_{ij} / 3 - \dot{\varepsilon}^{p}_{ij}) \tag{1}$$

where σ_{ij}, S_{ij} are the components of the stress tensor and stress deviator, respectively; P is the pressure; ε_{ij} and $\dot{\varepsilon}^{p}_{ij}$ are the total and plastic strain tensors; δ_{ij} is the Kronecker delta; K and μ are the bulk and shear moduli; α is the coefficient of thermal expansion; and T is the temperature. A superposed dot denotes differentiation with respect to time.

The Si-rich eutectic phase was assumed to behave as a linear isotropic elastic material. The deformation behavior of the aluminum phase was modeled within an isotropic elasto–plastic framework with damage. The plastic flow rule $\dot{\varepsilon}^{p}_{ij} = \dot{\lambda}S_{ij}$ was associative and based on the von Mises yield criterion $\sigma_{eq} - \sigma_{Yield}(\varepsilon^{p}_{eq}) = 0$, with the plastic multiplier λ being identically zero in the elastic stage. Isotropic strain hardening was described by an exponential function of the accumulated equivalent plastic strain ε^{p}_{eq}:

$$\sigma_{Yield} = \sigma_{s} - \left(\sigma_{s} - \sigma_{0}\right)\exp\left(-\varepsilon^{p}_{eq} / \varepsilon_{s}\right) \tag{2}$$

where σ_0 and σ_s are the initial yield strength and ultimate strength, respectively, and ε_s is the saturation strain.

A local damage model was introduced based on a critical value of accumulated equivalent plastic strain:

$$\varepsilon^{p}_{eq} = \varepsilon_{cr} \tag{3}$$

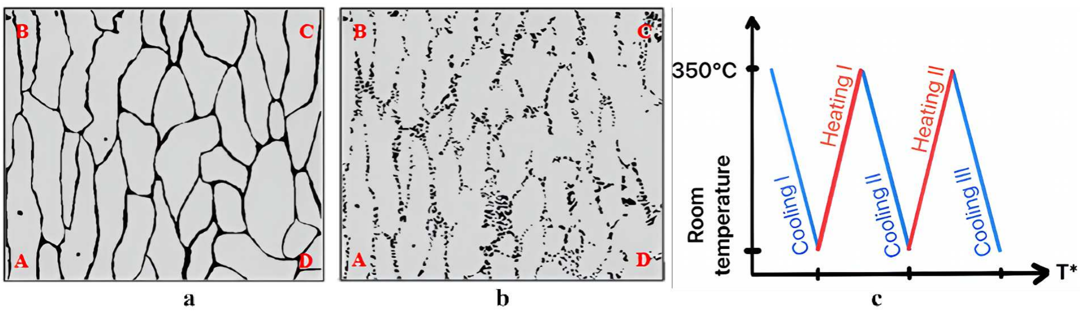

Fig. 4. (a) Microstructural models of LPBF AlSi10Mg with continuous, (b) discontinuous eutectic networks, (c) the scheme of thermal cycling.

Table 1. Material constants and model parameters.

	Young modulus (GPa)	Poisson coefficient	σ_0 (MPa)	σ_s (MPa)	ε_s	ε_{cr}	Coefficients of thermal expansion α, 10^{-5} K^{-1}
Si	160	0.225	-	-	-	-	0.25
Al	70	0.32	122	221	0.035	1	2.4

The damage evolution is abrupt rather than gradual. No progressive stiffness degradation is considered. Once the criterion (3) is satisfied, the corresponding finite element is considered damaged but is not removed from the mesh and retains its mass. Under conditions of volumetric tension ($\varepsilon_{kk} > 0$), both the pressure P and the stress deviator S_{ij} are set to zero in the damaged region. Under volumetric compression ($\varepsilon_{kk} < 0$), the material retains its ability to resist compressive stresses, and only the deviatoric stress component is set to zero. The model Eqs. (1) - (3) was implemented in ABAQUS/Explicit via a user-defined VUMAT subroutine.

In simulations of thermal cycling, boundary conditions reflected the physical scenario where the computational domain is surrounded by solidified material on its sides and by molten material on its top surface. Accordingly, symmetry conditions were prescribed on the BA, AD, and DC boundaries (see Fig. 4(a)), while the top surface was traction-free. The temperature was assumed to change uniformly throughout the domain, varying linearly from 350°C to room temperature during cooling and increasing linearly during heating according to the scheme in Fig. 4(c). After final cooling, uniaxial tensile loading was applied along the horizontal direction by imposing kinematic boundary conditions on the lateral boundaries, while the top and bottom boundaries remained free. The model parameters of the aluminum and Si-rich eutectic phases are presented in Table 1.

4. Results and Discussion

4.1. Microscale stress-strain evolution under thermal cycling

Microscale distributions of thermal-induced stresses formed in the beginning of the first cooling stage (Cooling I, Fig. 4(c)) are shown in Fig. 5. In both microstructural models, heterogeneous stresses arise at the early stage of cooling due to the mismatch in the coefficients of thermal expansion between the aluminum matrix and the Si-rich phase. In all cases, the stresses are higher in the eutectic phase and lower in the aluminum matrix, while the local stress magnitudes and spatial heterogeneity strongly depend on the eutectic network morphology.

A comparison of the equivalent stress fields within the Si-rich regions at the onset of Cooling I (Figs. 5(a) and 5(b)) indicates that local stresses in the continuous, vertically oriented Si-rich network walls (Fig. 5(b)) are approximately twice as high as those developing in the discontinuous eutectic network (Fig. 5(a)). In contrast, horizontally oriented continuous walls exhibit stress magnitudes comparable to, or lower than, those observed in the discontinuous network. In the aluminum matrix, a larger scatter of stress values is evident in the model with a discontinuous network (cf. Figs. 5(c) and (d)). The highest stress concentrations arise in the regions confined between vertically aligned Si-rich walls.

As the temperature decreases below approximately 320 °C, local stresses in the aluminum phase reach the yield strength, triggering the onset of plastic deformation. In the model featuring a discontinuous network, plastic strain localizes predominantly in the regions between vertically aligned Si-rich walls, where the aluminum experiences combined horizontal tension and vertical compression (Fig. 6(a)). By contrast, in the model with a continuous network, plastic deformation initiates at a later stage and concentrates mainly along the aluminum–eutectic interfaces, while the majority of aluminum cells remain under biaxial tension (Fig. 6(b)).

Figure 7 shows equivalent stress fields in the end of Cooling I (a, d), Heating I (b, e) and Cooling II (c, f) stages. Note that the type III residual stresses are considered to be those remaining after total cooling to room temperature. The Si-rich phase undergoes compression in vertical eutectic walls and tension in their horizontal segments (Figs. 7(a) to (d)). Plastic strains accumulated during cooling to room temperature led to the formation of type III residual stresses. The highest stresses develop in the vertical eutectic walls of the continuous network (Figs. 7(d)), while horizontal walls exhibit stress levels comparable to those in discontinuous network (Figs. 7(a) and (d)).

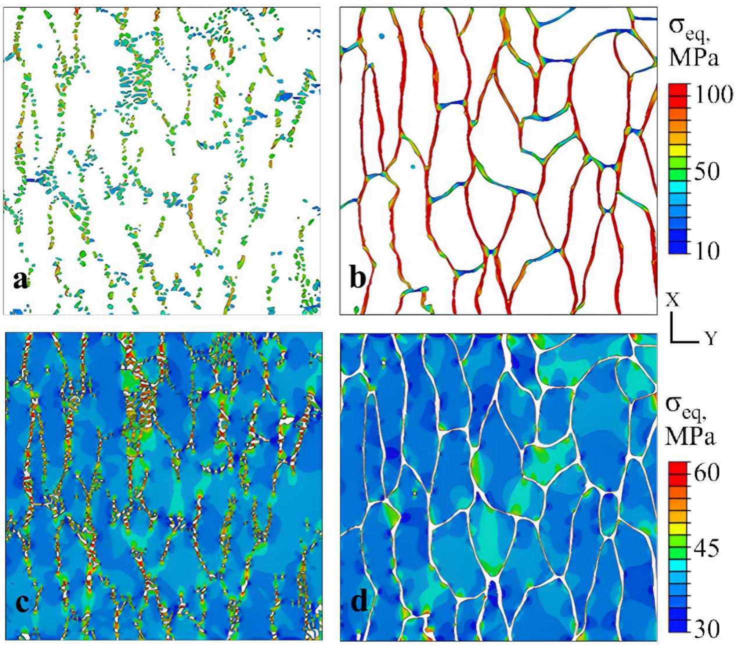

Fig. 5. Equivalent stress fields in microstructural models of LPBF AlSi10Mg with discontinuous (a, c) and continuous Si-rich networks (b, d) in Si-rich eutectic (a, b) and Al (c, d) phases in the beginning of first cooling cycle from 350 ℃ to 325 ℃ (elasticity).

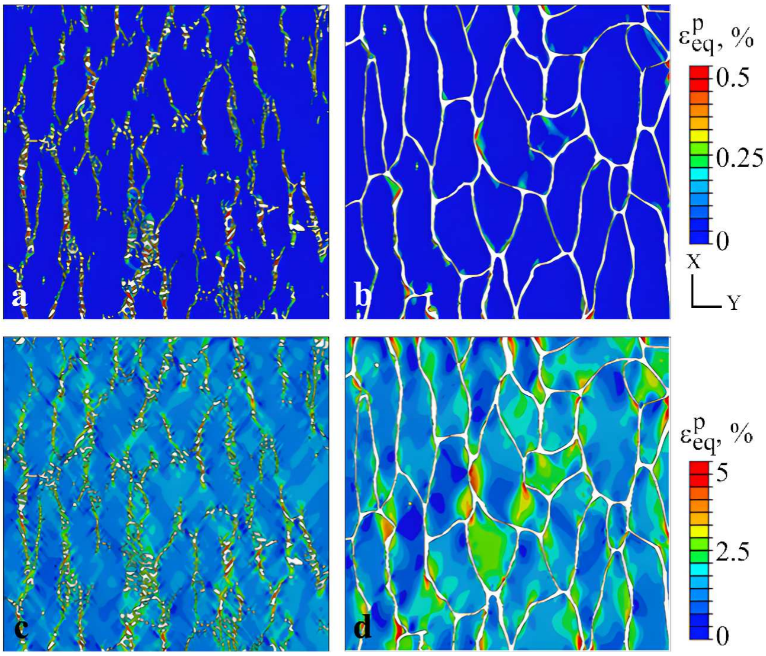

Fig. 6. Equivalent plastic strain fields of LPBF AlSi10Mg with discontinuous (a, c) and continuous Si-rich networks (b, d) after cooling from 350°C to 280°C (a, c) and from 280°C (c, d) to ambient temperature.

While the evolution of average plastic strain during thermal cycling is similar in both models, the localization patterns differ markedly (Figs. 7 and 8(c)). The first cooling cycle produces the largest increment of equivalent plastic strain (~0.6%), while subsequent cycles produce smaller strain increments (~0.4%), primarily during the second half of each cycle. The reduction in plastic strain increments during subsequent cycles is associated with strain hardening of the aluminum matrix caused by the plastic deformation accumulated during the preceding cycles. Local plastic strain magnitudes scale proportionally with the average value. At the end of cycling, the highest strains are localized within aluminum cells in the continuous network and between vertically aligned silicon particles in the discontinuous network.

Figure 8 shows the evolution of the equivalent stresses (Figs. 8(a) and (b)) and equivalent plastic strains (Fig. 8(c)) for both microstructural models during thermal cycling. The notation <·> denotes volume-averaged values over the computational domain. All variables are plotted as a function of the normalized time $T^* = T \cdot T_{total}^{-1}$, where T_{total} is the total time of thermal cycling. In the end of the first cooling cycle, the average equivalent stress reaches ~210 MPa in the model with a continuous network and 150 MPa in the model with a discontinuous network (Figs. 8(a) and (b)). During subsequent thermal cycles, the average stress decreases to a minimum in the middle of each cycle and then increases again, approaching the yield strength of the aluminum phase. In the model with a discontinuous network, the stress pattern during cooling and heating is nearly symmetric (Fig. 8(b)). In contrast, the model with a continuous network exhibits markedly asymmetric stress pattern between the cooling and heating stages (Fig. 8(a)).

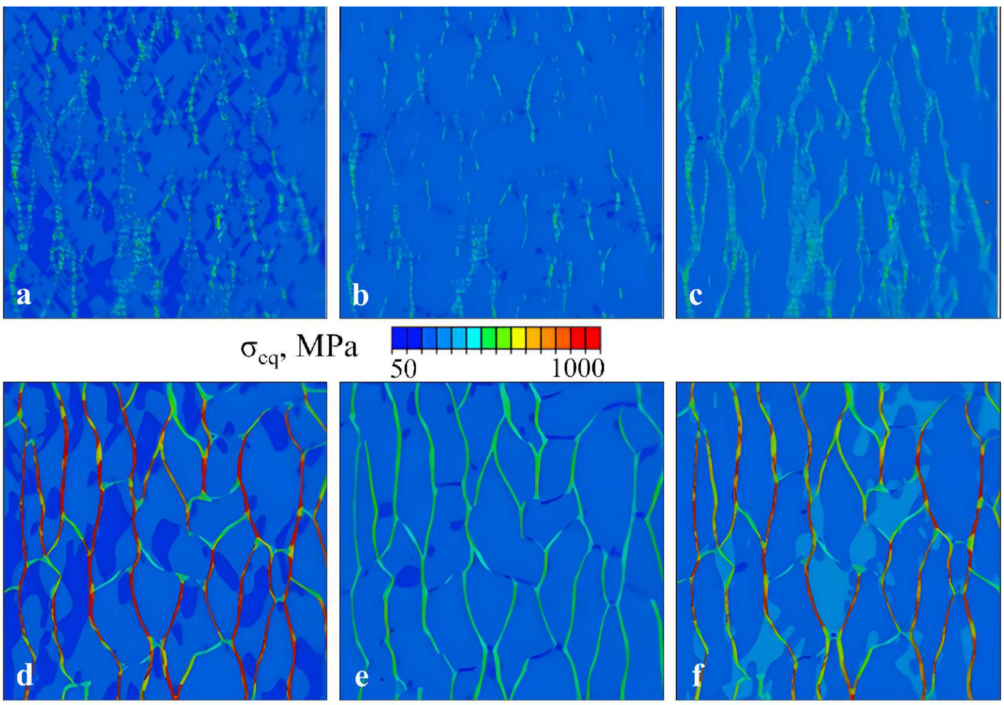

Fig. 7. Equivalent stress fields in microstructural models with discontinuous (a-c) and continuous Si-rich networks (d-f) in the end of Cooling I (a, d), Heating I (b, e) and Cooling II (c, f) stages.

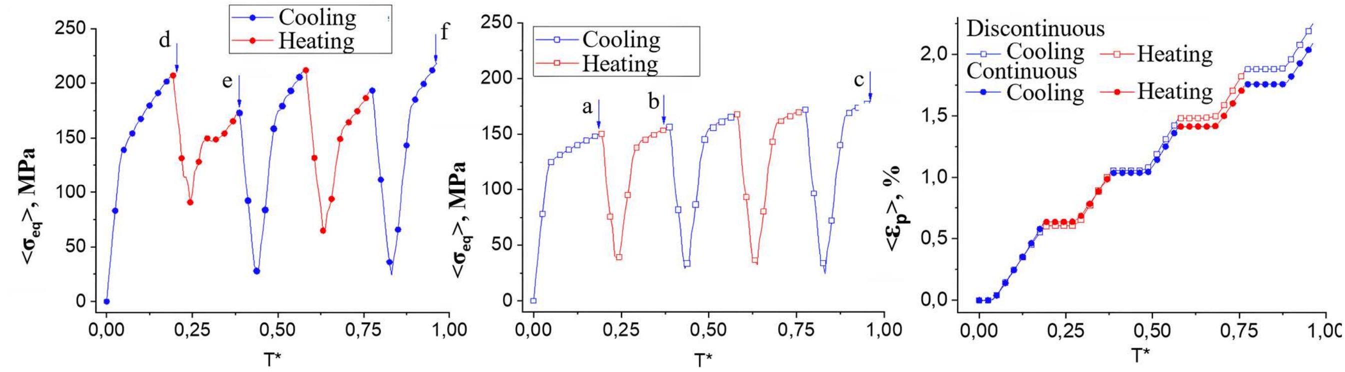

Fig. 8. Evolution of equivalent stresses (a, b) and plastic strain (c) in microstructural models with continuous (a) and discontinuous (b) Si-rich networks while thermocycling.

Analysis of the stress tensor components, σ_{xx} and σ_{yy}, acting parallel and perpendicular to the free surface reveals the origin of this asymmetry. Distributions of these stress tensor components at the end of the first cooling and subsequent heating are shown in Figs. 9 and 10. Negative (compressive) and positive (tensile) stress values are represented by blue and red colors, respectively, and green color corresponds to the zero stress.

In the aluminum phase of both models the stress σ_{xx} is tensile after cooling and compressive after heating (Fig. 9). Because the eutectic network is discontinuous, the aluminum cells are not mechanically constrained in the vertical direction and can accommodate thermal strains through local deformation, preventing the development of significant σ_{yy} stresses. The evolution of the normal stress component σ_{yy}, oriented perpendicular to the free surface differs markedly between the two models and is central to understanding the asymmetric average stress development. In the model with a discontinuous Si-rich network (Figs. 10(a) to (c)), σ_{yy} remains close to zero within the interiors of the aluminum cells during both cooling and heating, as indicated by the predominance of green regions. Local tensile and compressive stresses arise only in the vicinity of silicon particles, where the thermal expansion mismatch generates stress concentrations (red and blue regions). However, these localized fluctuations largely self-equilibrate, leading to a negligible contribution to the macroscopic σ_{yy} component.

In contrast, the model containing a continuous Si-rich network (Figs. 10(b) and (d)) demonstrates a fundamentally different stress evolution. At the end of cooling, pronounced tensile σ_{yy} stresses develop within the aluminum cells. Simultaneously, compressive σ_{yy} stresses are concentrated in the vertically aligned Si-rich walls (Fig. 10(b)). This stress partitioning reflects the strong mechanical constraint imposed by the continuous network, which restricts out-of-plane contraction of the aluminum matrix. During the subsequent heating stage, a stress reversal occurs in the Si-rich walls, accompanied by significant stress relaxation within the aluminum cells (Fig. 10(d)).

A more rigorous quantitative analysis includes statistical evaluation of the simulated fields. The statistical analysis of the stress and strain fields is provided in terms of frequency counts constructed separately for Al and Si-rich phases. Calculating frequency count for a certain quantity involves the following procedure. The range of the value variation in the computational domain is divided into a set of equal-width intervals (bins) specific for each phase. Then, the number of finite elements experiencing the values falling within each interval is counted. The resulting frequency count distributions characterize how widely the quantity is spread across the microstructure.

In our study, the frequency curves provide statistical descriptions of the spatial heterogeneity of the stress–strain state. Specifically for Gaussian distributions, the peaks in the frequency curves typically correspond to the mean. The narrower the peaks, the larger the number of elements experiencing values close to the mean, whereas the broader peaks reflect wider scatter of the values about the mean.

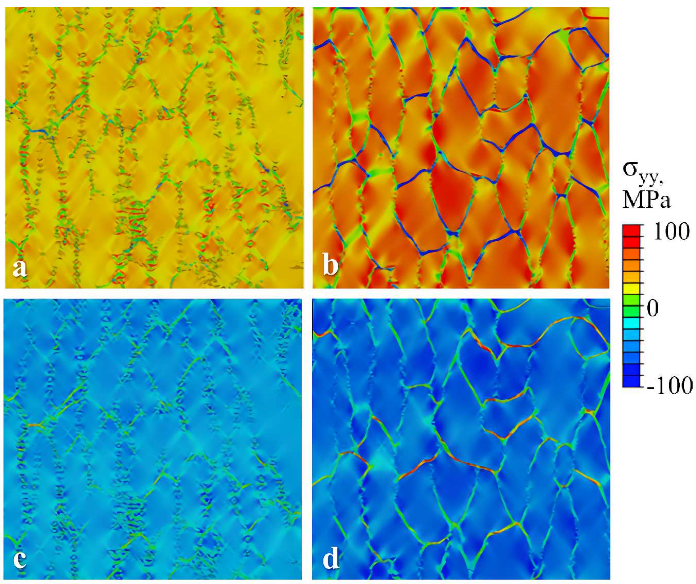

Fig. 9. σ_{xx} stress fields in microstructural models with discontinuous (a, c) and continuous (b, d) Si-rich networks in the end of the first cooling (a, b) and heating (c, d) cycles.

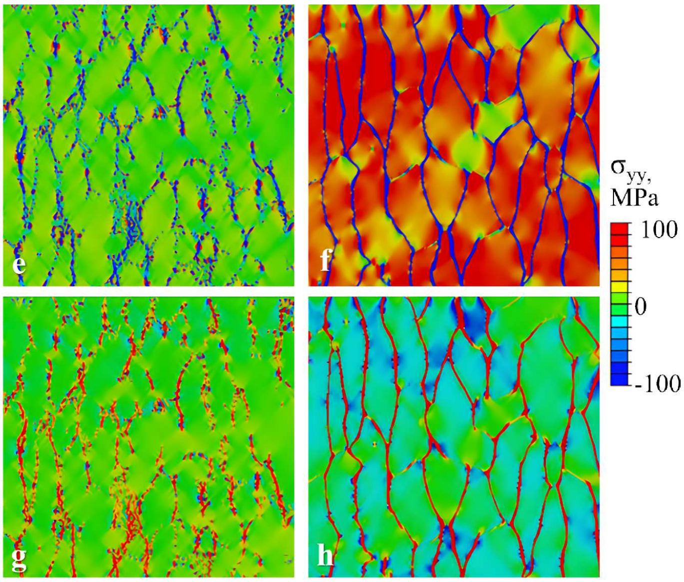

Fig. 10. σ_{yy} stress fields in microstructural models with discontinuous (a, c) and continuous (b, d) Si-rich networks in the end of first cooling (a, b) and heating (c, d) cycles.

The frequency curves for both equivalent plastic strain (Figs. 11(c) to (f)) and equivalent stress (Figs. 11(a) and (d)) in the aluminum phase display a similar behavior for the two microstructural models. During thermal cycling, the distributions remain unimodal and close to normal (Gaussian-like). With each successive cycle, the peaks systematically shift toward higher values, reflecting progressive accumulation of plastic deformation and increasing stress levels in the aluminum matrix. At the same time, peaks in the distribution curves broaden, indicating an increasing scatter of local values around the mean. Although this general trend is common to both morphologies, the model with a discontinuous eutectic network demonstrates peaks that are nearly twice as high and somewhat narrower compared to the continuous network. This behavior signifies a more concentrated distribution of stress and strain values and a lower degree of spatial scatter within the aluminum phase in the discontinuous network.

The stress distributions for the Si-rich phases in the two models differ markedly (cf. curves Figs. 11(b) and (e)). For the discontinuous network model, the frequency curves show unimodal, near-normal distributions; notably, while the peak amplitudes and widths vary between the cooling and heating cycles, their locations on the stress axis remain unchanged (Fig. 11(b)). In contrast, for the model with a continuous network (Fig. 11(e)), the frequency distributions corresponding is noticeably narrower for the heating stages, indicating partial stress relaxation in a portion of elements. After cooling, the peaks in the curves broaden, acquiring a distinctly bimodal form. Comparison with the corresponding stress fields (Fig. 5) suggests that this bimodality arises from a pronounced stress partitioning between vertically and horizontally oriented eutectic walls. The high-stress mode corresponds to the vertically aligned walls, whereas the low-stress mode is associated with the horizontal segments of the network. Vertically oriented eutectic walls experience strong constraint and carry higher stresses, whereas horizontal segments remain less constrained and sustain lower stresses.

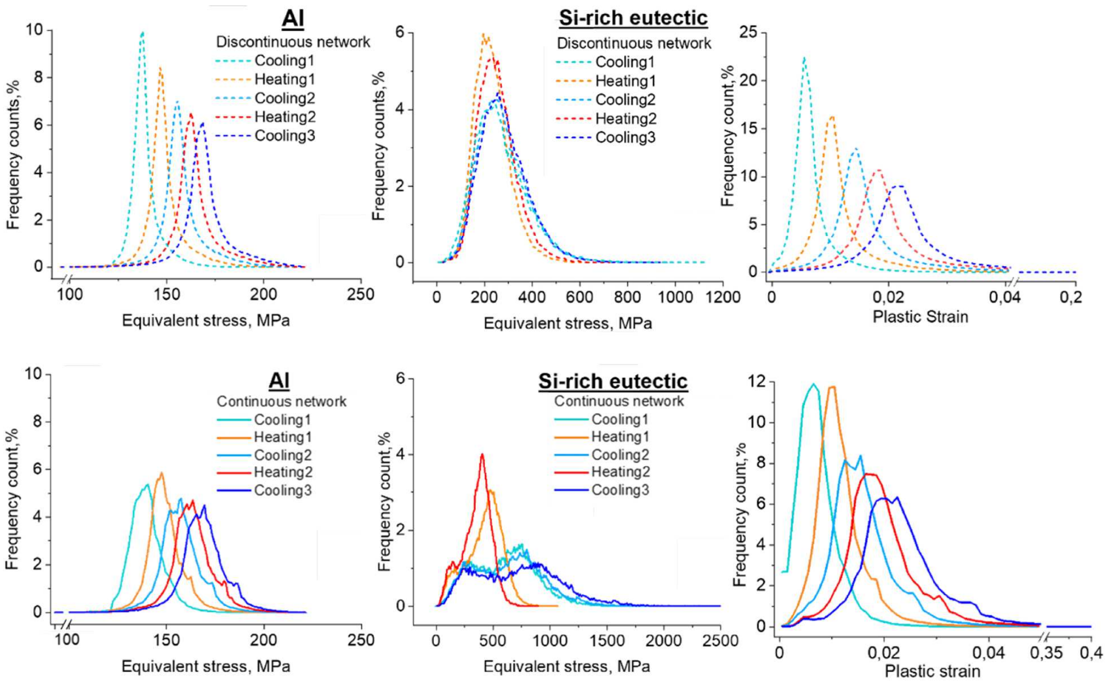

Fig. 11. Frequency count curves of equivalent stresses (a, b, d, e) and plastic strains (c, f) at the end of each stage in Al (a, d, c, f) and Si-rich (b, e) phases in microstructural models with discontinuous (a-c) and continuous (d-f) Si-rich networks.

Overall, the numerical results demonstrate that the morphology of the Si-rich eutectic network plays a significant role in the formation and evolution of intragranular thermal residual stresses. A continuous network acts as a rigid skeleton that constrains matrix deformation, promotes stress concentration, and leads to anisotropic and strongly heterogeneous type III residual stress fields. In contrast, a discontinuous network allows local accommodation through matrix plasticity. Consequently, Si-rich morphology governs not only the magnitude but also the spatial distribution and statistical characteristics of type III residual stresses, which are expected to influence subsequent mechanical response.

4.2. Influence of microscale residual stresses on deformation response of LPBF-fabricated AlSi10Mg

The most important consequence of thermal-induced residual stresses is that they introduce a pre-strained state before the onset of external loading. To isolate and clearly demonstrate the potential contribution of type III residual stresses to the deformation behavior, two tensile loading scenarios were considered for each Si-rich eutectic morphology: (i) loading with predefined residual stress fields inherited from thermal cycling, and (ii) loading from a residual stress-free initial state under otherwise identical boundary conditions and material parameters.

Figure 12(a) shows the calculated tensile curves plotted in terms of volume-averaged equivalent stress $<\sigma_{eq}>$ versus tensile strain. The stress values $<\sigma_{eq}>$ were obtained using equation:

$$<\sigma_{eq}> = \frac{\sum_n [\sigma_{eq} V]^n}{\sum_n V^n}, \; n = 1 \dots N \tag{4}$$

where V is the volume of the n-th element and N is the number of elements in the computational domain, $n = 1 \dots N$. The tensile strain was calculated as a ratio between displacement and initial length of the model in tensile direction.

The tensile curves calculated with and without predefined residual stress fields are nearly similar in shape but shifted relative to each other by a value of plastic strain accumulated during thermal cycling (~ 2.2%, Fig. 12(a)). This means that the effect of residual stresses can be interpreted primarily as a pre-straining of the material prior to tensile loading. In other words, the microstructure containing residual stresses behaves as if it has already undergone about 2.2% plastic deformation before the external load is applied. As a consequence, the remaining tensile ductility is reduced by approximately 2.2%. Considering that the experimentally reported ductility of LPBF AlSi10Mg typically varies between 1 and 8%, this reduction represents a substantial fraction of the observed scatter. The yield strength respectively increases due to the strain hardening in the aluminum matrix (Fig. 12(b)). A comparison of the mechanical responses associated with different Si-rich network morphologies reveals that the microstructure with a continuous network exhibits a higher strain hardening rate and a lower ultimate strain than that with a discontinuous network. These results are consistent with the experimental observations reported in the literature [29–31].

The fracture behavior of the models containing predefined residual stresses is examined below. Illustrative snapshots of plastic strain fields and crack evolution corresponding to the drop portion in the stress-strain curves are compared in Fig. 13 for the models with different morphology of the Si-rich network. The a-c and d-f labels in the curves (Fig. 12(b)) indicate the strain levels for which the snapshots are presented in subfigures Figs. 13(a) to (c) and Figs. 13(d) to (f), respectively. In both models, fracture is initiated in the aluminum phase in the interfacial regions and proceeds through several stages (Fig. 13). In the model with a discontinuous network, a set of isolated microcracks (marked by ellipses in Fig. 13(a)) is formed between Si-rich segments within bands of localized plastic deformation, particularly at intersections of these bands with the Si-rich eutectic walls (Fig. 14(a)) as observed experimentally in [39]. The cracks nucleating within the most intense deformation bands start to propagate toward each other and eventually coalesce, forming a dominant through-thickness crack (Figs. 12(b) and (c)).

In the model with a continuous eutectic network, microcracks nucleate along Si-rich walls (marked by ellipses in Fig. 13(d)) but propagate preferentially along aluminum–silicon interfaces. At an advanced loading stage, crack is governed primarily by fracture in interfacial regions of intense plastic strain. The resulting crack paths are more branched (cf. crack propagations on Figs. 13(d) and (e)), reflecting the stronger mechanical constraint imposed by the continuous eutectic network and the associated nonhomogeneous stress distribution.

A qualitatively similar fracture scenario develops in the models with a stress-free initial state (compare pairwise equivalent plastic strain fields in Figs. 13(c) and 14(a), and Figs. 13(f) and 14(b)). However, in this case crack initiation is postponed. The present simulations demonstrate that residual stresses influence the mechanical response of LPBF-fabricated metals, amplifying the effects of microstructural morphology. Specifically, the regions with continuous Si-rich eutectic network are characterized by higher yield strength and lower ductility than those with a discontinuous network.

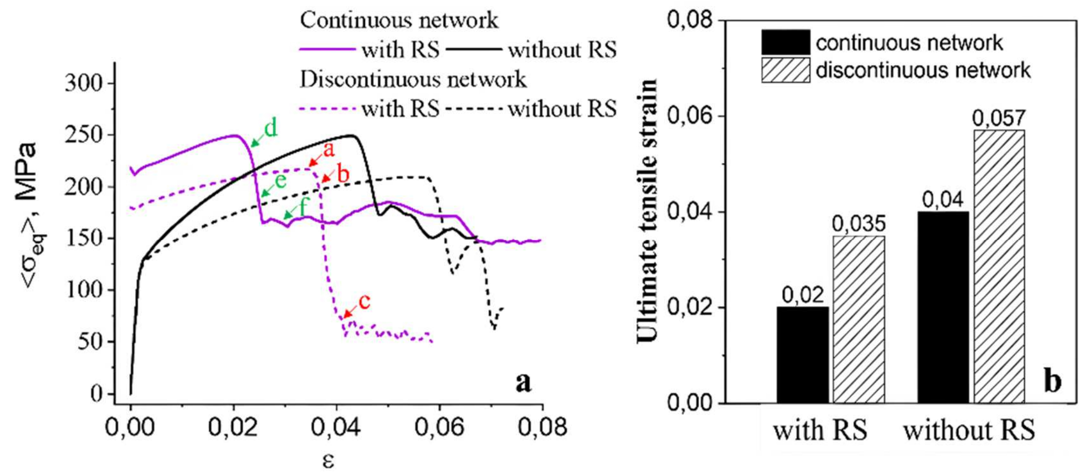

Fig. 12. Simulated stress-strain curves, (a) and ultimate strain histograms (b) for the microstructural models with and without predefined residual stress fields.

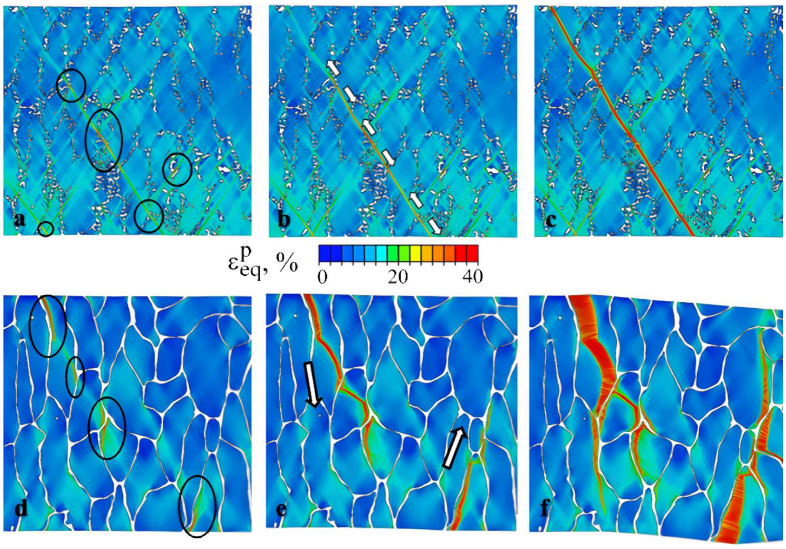

Fig. 13. Equivalent plastic strain distributions in microstructural models with discontinuous (a-c) and continuous Si-rich networks (d-f) under uniaxial tension with predefined residual stress fields.

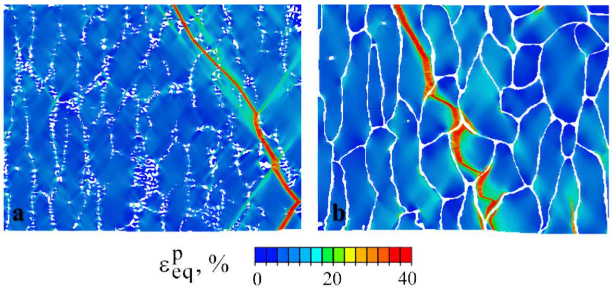

Fig. 14. Equivalent plastic strain fields in microstructural models with discontinuous (a-c) and continuous Si-rich eutectic networks (d-f) under uniaxial tension with a stress-free initial state.

Experimental studies have demonstrated that crack propagation in LPBF-fabricated materials depends on the loading direction relative to the build direction (BD). This anisotropy has frequently been attributed to microstructure morphology and high residual stresses at melt pool boundaries [40]. In particular, melt pool boundaries were suggested to exhibit lower cohesive strength than grain boundaries, thereby facilitating crack propagation [41]. An alternative interpretation proposed that the anisotropy originates primarily from the cellular-dendritic substructure itself, as loading along BD involves a higher fraction of eutectic framework boundaries aligned with the tensile axis [42], a view supported by numerical studies emphasizing the role of cellular morphology in strain localization and fracture [37, 43].

5. Conclusion

In the present study, the formation of intragranular type III residual stresses during LPBF-relevant thermal cycling and their influence on the subsequent tensile response of AlSi10Mg have been investigated. Two representative cellular-dendritic morphologies were considered, corresponding to continuous and discontinuous Si-rich eutectic networks.

Thermal cycling was shown to lead to the development of pronounced microscale residual stresses caused by the mismatch in thermal expansion and elastoplastic response between the aluminum matrix and the Si-rich phase. The magnitude, spatial distribution, and statistical characteristics of these stresses are strongly governed by eutectic network morphology. A continuous Si-rich network imposes stronger mechanical constraint on the aluminum cells, resulting in higher average equivalent stresses, marked stress partitioning between vertical and horizontal network segments, and bimodal stress distributions after cooling. In contrast, a discontinuous network promotes partial stress relaxation due to plastic deformation in the Al phase.

Plastic strain accumulation during thermal cycling is comparable in terms of average values for both morphologies; however, localization patterns differ significantly. In the continuous network, plastic strain localizes along aluminum–eutectic interfaces and within constrained cells, whereas in the discontinuous network it localizes preferentially between Si-rich segments. The first cooling cycle produces the largest increment of plastic strain, while subsequent cycles contribute progressively smaller increments.

Incorporation of the thermally induced residual stresses into tensile simulations demonstrates that their primary mechanical effect is equivalent to pre-straining of the material by approximately 2.2%. The tensile curves obtained with and without residual stresses coincide after shifting by this pre-accumulated strain. Accordingly, residual stresses reduce the available ductility while increasing the initial yield strength. Also, residual stresses accelerate crack initiation due to the superposition of internal and externally applied stress fields.

The fracture mechanisms are shown to depend significantly on the eutectic morphology. The discontinuous eutectic network promotes crack nucleation within localized deformation bands and subsequent coalescence into a dominant through-thickness crack. The continuous network, characterized by stronger constraint and higher residual stress concentrations, leads to more branched and tortuous crack paths along aluminum–silicon interfaces.

Overall, the results demonstrate that cellular-dendritic morphology and intragranular residual stresses are key, interrelated factors governing deformation and fracture in LPBF-fabricated AlSi10Mg. While melt pool boundaries are often considered the principal source of anisotropy and crack susceptibility, the present findings indicate that sub-grain architecture and microscale residual stress fields play an equally critical role in controlling strain localization and failure. Explicit consideration of these factors is therefore essential for predictive modeling and microstructure-informed optimization of additively manufactured aluminum alloys.

Author Contributions

E. Dymnich carried out the investigation, curated the data, prepared the original draft and its subsequent review and editing, and created the visualizations. V. Romanova conceived the study, developed the methodology, performed the formal analysis, curated the data, and prepared the original draft of the manuscript, as well as contributed to its review and editing. V. Shakhidzhanov carried out the investigation, performed validation, and contributed to the visualizations. V. Balokhonov conducted the investigation and contributed to the visualizations. A. Borodina performed validation and contributed to the visualizations. R. Balokhonov contributed to conceptualization, methodology development, formal analysis, and investigation. All authors discussed the results, reviewed, and approved the final version of the manuscript.

Acknowledgments

Not applicable.

Conflict of Interest

The authors declared no potential conflicts of interest concerning the research, authorship, and publication of this article.

Funding

The work was performed according to the Government research assignment for ISPMS SB RAS, project FWRW-2026-0003.

Data Availability Statements

Not applicable.

References

[1] Arumugaprabu, V., Arunprasath, K., Rajendran, S., Yang, Y.-L., Aravindan, S., Impact of additive manufacturing techniques on metal based composites: a brief review, *Discover Materials*, 5, 2025, 237.

[2] Li, Z., Ruan, H., Li, M., Yu, C., Jia, Q., Wang, J., Chen, L., Additive manufacturing: prospects and diverse applications, *Metals*, 15, 2025, 158.

[3] Liović, D., Franulović, M., Ferlič, L., Gubeljak, N., Surface roughness of Ti6Al4V alloy produced by laser powder bed fusion, *Facta Universitatis, Series: Mechanical Engineering*, 22, 2024, 063.

[4] Zinovieva, O., Romanova, V., Dymnich, E., Zinoviev, A., Balokhonov, R., A review of computational approaches to the microstructure-informed mechanical modelling of metals produced by powder bed fusion additive manufacturing, *Materials*, 16, 2023, 6459.

[5] Prasad, K., Obana, M., Ishii, Y., Ito, A., Torizuka, S., The effect of laser scanning strategies on the microstructure, texture and crystallography of grains exhibiting hot cracks in additively manufactured Hastelloy X, *Mechanics of Materials*, 157, 2021, 103816.

[6] Xie, J.W., Fox, P., O'Neill, W., Sutcliffe, C.J., Effect of direct laser re-melting processing parameters and scanning strategies on the densification of tool steels, *Journal of Materials Processing Technology*, 170, 2005, 516-523.

[7] Zinovieva, O., Romanova, V., Balokhonov, R., Effects of scanning pattern on the grain structure and elastic properties of additively manufactured 316L austenitic stainless steel, *Materials Science and Engineering: A*, 832, 2022, 142447.

[8] Zhao, L., Song, L., Santos Macías, J.G., Zhu, Y., Huang, M., Simar, A., Li, Z., Review on the correlation between microstructure and mechanical performance for laser powder bed fusion AlSi10Mg, *Additive Manufacturing*, 56, 2022, 102914.

[9] Karthik, G.M., Kim, H.S., Heterogeneous aspects of additive manufactured metallic parts: a review, *Metals and Materials International*, 27, 2021, 1-39.

[10] Tonelli, L., Revealing the hierarchical microstructure of innovative additively manufactured metal parts with conventional light microscopy, *Metallography, Microstructure, and Analysis*, 10, 2021, 278-282.

[11] Balokhonov, R., Utyaganova, V., Gatiyatullina, D., Zemlianov, A., Romanova, V., Interlayer effect on deformation and fracture of dendritic structure formed during wire-feed electron-beam additive manufacturing of Al-Si alloy, *Facta Universitatis, Series: Mechanical Engineering*, 22, 2024, 515.

[12] Prashanth, K.G., Eckert, J., Formation of metastable cellular microstructures in selective laser melted alloys, *Journal of Alloys and Compounds*, 707, 2017, 27-34.

[13] Brandl, E., Heckenberger, U., Holzinger, V., Buchbinder, D., Additive manufactured AlSi10Mg samples using selective laser melting (SLM): microstructure, high cycle fatigue, and fracture behavior, *Materials & Design*, 34, 2012, 159-169.

[14] Zemlyanov, A.V., Gatiyatullina, D.D., Utyaganova, V.R., Dymnich, E., Shamarin, N.N., Nikonov, S.Yu., Romanova, V.A., Kulkov, A.S., Balokhonov, R.R., A study of deformation and fracture of the eutectic in an additively manufactured Al-Si composite alloy, *Physical Mesomechanics*, 26, 2023, 678-690.

[15] Kim, D.-K., Woo, W., Hwang, J.-H., An, K., Choi, S.-H., Stress partitioning behavior of an AlSi10Mg alloy produced by selective laser melting during tensile deformation using in situ neutron diffraction, *Journal of Alloys and Compounds*, 686, 2016, 281-286.

[16] Kim, D.-K., Hwang, J.-H., Kim, E.-Y., Heo, Y.-U., Woo, W., Choi, S.-H., Evaluation of the stress-strain relationship of constituent phases in AlSi10Mg alloy produced by selective laser melting using crystal plasticity FEM, *Journal of Alloys and Compounds*, 714, 2017, 687-697.

[17] Meier, C., Penny, R.W., Zou, Y., Gibbs, J.S., Hart, A.J., Thermophysical phenomena in metal additive manufacturing by selective laser melting: fundamentals, modeling, simulation and experimentation, *Annual Review of Heat Transfer*, 20, 2017, 241-316.

[18] Zhu, K., Song, L., Zhao, L., Zhu, Y., Liang, S., Huang, M., Li, Z., Numerical study on the effect of crystallographic orientation on mechanical behavior and its anisotropy of laser powder bed fusion AlSi10Mg, *Journal of Alloys and Compounds*, 976, 2024, 173284.

[19] Wang, Y.M., Voisin, T., McKeown, J.T., Ye, J., Calta, N.P., Li, Z., Zeng, Z., Zhang, Y., Chen, W., Roehling, T.T., Ott, R.T., Santala, M.K., Depond, P.J., Matthews, M.J., Hamza, A.V., Zhu, T., Additively manufactured hierarchical stainless steels with high strength and ductility, *Nature Materials*, 17, 2018, 63-71.

[20] Takata, N., Kodaira, H., Sekizawa, K., Suzuki, A., Kobashi, M., Change in microstructure of selectively laser melted AlSi10Mg alloy with heat treatments, *Materials Science and Engineering: A*, 704, 2017, 218-228.

[21] Chen, B., Moon, S.K., Yao, X., Bi, G., Shen, J., Umeda, J., Kondoh, K., Strength and strain hardening of a selective laser melted AlSi10Mg alloy, *Scripta Materialia*, 141, 2017, 45-49.
[22] Gamin, Yu.V., Korotitskii, A.V., Kin, T.Yu., Galkin, S.P., Kostin, S.A., Tikhomirov, E.O., Development of temperature-speed modes of hot deformation of Co-28Cr-6Mo alloy based on processing maps, *Izvestiya Vysshikh Uchebnykh Zavedeniy, Chernaya Metallurgiya*, 65, 2022, 786-797.
[23] Köhnen, P., Létang, M., Voshage, M., Schleifenbaum, J.H., Haase, C., Understanding the process-microstructure correlations for tailoring the mechanical properties of L-PBF produced austenitic advanced high strength steel, *Additive Manufacturing*, 30, 2019, 100914.
[24] Saeidi, K., Gao, X., Zhong, Y., Shen, Z.J., Hardened austenite steel with columnar sub-grain structure formed by laser melting, *Materials Science and Engineering: A*, 625, 2015, 221-229.
[25] Megahed, M., Mindt, H.-W., N'Dri, N., Duan, H., Desmaison, O., Metal additive-manufacturing process and residual stress modeling, *Integrating Materials and Manufacturing Innovation*, 5, 2016, 61-93.
[26] Daoud, M.E., Taha, I., Abdelgawad, A., Barsoum, I., Khan, K.A., Anjum, D.H., Mapping residual stresses in AlSi10Mg alloy fabricated by powder bed fusion-laser beam method, *Scientific Reports*, 15, 2025, 24784.
[27] Carpenter, K., Tabei, A., On residual stress development, prevention, and compensation in metal additive manufacturing, *Materials*, 13, 2020, 255.
[28] Lindroos, M., Pinomaa, T., Antikainen, A., Lagerbom, J., Reijonen, J., Lindroos, T., Andersson, T., Laukkanen, A., Micromechanical modeling approach to single track deformation, phase transformation and residual stress evolution during selective laser melting using crystal plasticity, *Additive Manufacturing*, 38, 2021, 101819.
[29] Sajadi, F., Tiemann, J.-M., Bandari, N., Cheloee Darabi, A., Mola, J., Schmauder, S., Fatigue improvement of AlSi10Mg fabricated by laser-based powder bed fusion through heat treatment, *Metals*, 11, 2021, 683.
[30] Salvati, E., Evaluating fatigue onset in metallic materials: problem, current focus and future perspectives, *International Journal of Fatigue*, 188, 2024, 108487.
[31] Neto, D.M., Borges, M.F., Sérgio, E.R., Antunes, F.V., Effect of residual stresses on fatigue crack growth: a numerical study based on cumulative plastic strain at the crack tip, *Materials*, 15, 2022, 2156.
[32] Yan, X., Yang, X., Tian, G., Sun, D., Liu, S., Xiong, Z., Wen, Z., Xu, Q., Modeling and simulation investigations on microstructure evolution during additive manufacturing of AlSi10Mg alloy, *Metals*, 12, 2022, 1711.
[33] Nammalvar Raja Rajan, A., Krochmal, M., Wegener, T., Biswas, A., Hartmaier, A., Niendorf, T., Moeini, G., Micromechanical modeling of AlSi10Mg processed by laser-based additive manufacturing: from as-built to heat-treated microstructures, *Materials*, 15, 2022, 5562.
[34] Hadadzadeh, A., Baxter, C., Amirkhiz, B.S., Mohammadi, M., Strengthening mechanisms in direct metal laser sintered AlSi10Mg: comparison between virgin and recycled powders, *Additive Manufacturing*, 23, 2018, 108-120.
[35] Takata, N., Liu, M., Hirata, M., Suzuki, A., Kobashi, M., Kato, M., Adachi, H., Microstructural origins of high strength of Al-Si alloy manufactured by laser powder bed fusion: in-situ synchrotron radiation X-ray diffraction approach, *Journal of Materials Science & Technology*, 178, 2024, 80-89.
[36] Bisht, M.S., Gaur, V., Singh, I.V., A study of strengthening and hardening micro-mechanisms in additively built AlSi10Mg using crystal plasticity simulations, *Metals and Materials International*, 31, 2025, 2855-2874.
[37] Romanova, V., Balokhonov, R., Borodina, A., Zinovieva, O., Dymnich, E., Fortuna, S., Shugurov, A., Micromechanical study of intragranular stress and strain partitioning in an additively manufactured AlSi10Mg alloy, *Thin-Walled Structures*, 196, 2024, 111464.
[38] Liu, X., Zhao, C., Zhou, X., Shen, Z., Liu, W., Microstructure of selective laser melted AlSi10Mg alloy, *Materials & Design*, 168, 2019, 107677.
[39] Zhao, L., Santos Macías, J.G., Douillard, T., Li, Z., Simar, A., Unveiling damage sites and fracture path in laser powder bed fusion AlSi10Mg: comparison between horizontal and vertical loading directions, *Materials Science and Engineering: A*, 807, 2021, 140845.
[40] Jiang, Z., Li, Y., Luo, H., Zhou, B., Liang, Y., Liang, Y., Effect of the boundary orientation of melt pool on mechanical property and fracture path in selective-laser-melted AlSi10Mg alloy, *Metals and Materials International*, 28, 2022, 2934-2946.
[41] Shifeng, W., Shuai, L., Qingsong, W., Yan, C., Sheng, Z., Yusheng, S., Effect of molten pool boundaries on the mechanical properties of selective laser melting parts, *Journal of Materials Processing Technology*, 214, 2014, 2660-2667.
[42] Zhang, X.X., Andrä, H., Crystal plasticity simulation of the macroscale and microscale stress-strain relations of additively manufactured AlSi10Mg alloy, *Computational Materials Science*, 200, 2021, 110832.
[43] Romanova, V., Borodina, A., Dymnich, E., Balokhonov, V., Balokhonov, R., Influence of cellular dendritic structure and grain orientation on deformation behavior of additively manufactured AlSi10Mg alloy, *Russian Physics Journal*, 67, 2024, 1668-1676.

ORCID iD

Ekaterina Dymnich https://orcid.org/0000-0002-8525-8443
Varvara Romanova https://orcid.org/ 0000-0001-8693-3810
Valeriy Shakhidzhanov https://orcid.org/0009-0001-0989-7454
Vasiliy Balokhonov https://orcid.org/0009-0000-9324-5629
Anzhelika Borodina https://orcid.org/0009-0005-2899-8727
Ruslan Balokhonov https://orcid.org/0000-0001-9994-5685

How to cite this article: Dymnich E., Romanova V., Shakhidzhanov V., Balokhonov V., Borodina A., Balokhonov R. Thermal-Induced Intragranular Residual Stresses in LPBF AlSi10Mg and Their Impact on Mechanical Response, *J. Appl. Comput. Mech.*, xx(x), 2026, 1–11. https://doi.org/10.22055/jacm.2026.49339.5910